IJMMM International Journal of Minerals, Metallurgy and Materials 矿物冶金与材料学报（英文版）

Flow zone distribution and mixing time in a Peirce–Smith copper converter

Hongliang Zhao, Jingqi Wang, Fengqin Liu, and Hong Yong Sohn

Cite this article as:
Hongliang Zhao, Jingqi Wang, Fengqin Liu, and Hong Yong Sohn, Flow zone distribution and mixing time in a Peirce–Smith copper converter, *Int. J. Miner. Metall. Mater.*, 29(2022), No. 1, pp. 70-77. https://doi.org/10.1007/s12613-020-2196-8

View the article online at SpringerLink or IJMMM Webpage.

International Journal of Minerals, Metallurgy and Materials
Volume 29, Number 1, January 2022, Page 70
https://doi.org/10.1007/s12613-020-2196-8

Flow zone distribution and mixing time in a Peirce–Smith copper converter

Hongliang Zhao[1,2,3)], *Jingqi Wang*[2)], *Fengqin Liu*[1,2)], *and Hong Yong Sohn*[3),✉]

1) State Key Laboratory of Advanced Metallurgy, University of Science and Technology Beijing, Beijing 100083, China
2) School of Metallurgical and Ecological Engineering, University of Science and Technology Beijing, Beijing 100083, China
3) Department of Materials Science and Engineering, The University of Utah, Salt Lake City, Utah 84112, USA
(Received: 29 June 2020; revised: 17 September 2020; accepted: 18 September 2020)

Abstract: Peirce–Smith copper converting involves complex multiphase flow and mixing. In this work, the flow zone distribution and mixing time in a Peirce–Smith copper converter were investigated in a 1:5 scaled cold model. Flow field distribution, including dead, splashing, and strong-loop zones, were measured, and a dimensionless equation was established to determine the correlation of the effects of stirring and mixing energy with an error of <5%. Four positions in the bath, namely, injection, splashing, strong-loop, and dead zones, were selected to add a hollow salt powder tracer and measure the mixing time. Injecting a quartz flux through tuyeres or into the backflow point of the splashing wave through a chute was recommended instead of adding it through a crane hopper from the top of the furnace to improve the slag-making reaction.

Keywords: Peirce–Smith converter; copper smelting; flow fields; mixing time; cold model experiments

1. Introduction

Copper matte converting process that involves complex gas–liquid–solid multiphase flows is one of the key processes in copper pyrometallurgy. The most widely used converting furnace for the production of blister copper from copper matte by blowing air or oxygen-enriched air through side-blown tuyeres is Peirce–Smith converter (PSC) [1−2]. The stirring and mixing effects in PSC are essential for slag- and copper-making reactions, gas utilization, and total converting efficiency. Operating parameters, such as tuyere diameter, liquid height, and gas flow rate are closely related to flow field distribution and material mixing effect in a molten bath [3−4].

Many researchers have focused on improving gas-blown smelting processes by investigating the flow field and mixing via cold model experiments and numerical simulations. Gas flow, which is the main energy input in the PSC, is injected through side-blown tuyeres. Ma *et al.* [5] illustrated the flow pattern of an injected gas through a side tuyere and established dimensionless equations for the jet spreading angle and penetration depth of the gas flow. During the PSC process, a surface splashing wave is an important factor associated with the stirring and mixing intensity. Vaarno *et al.* [6] simulated gas injection in the PSC and found that oxidation occurs mainly near a tuyere and generates the recirculatory flow of the matte phase. Thus, a large part of oxidation likely takes place during bubble formation. Hou *et al.* [7], E [8−9], and Wang *et al.* [10] investigated the mixed layers and raceways in a blast furnace (packed bed) via a DEM–CFD (Discrete Element Method and Computational Fluid Dynamics) method. They also comprehensively examined the effects of tuyere diameter and gas flow rate. Other researchers explored heat transfer during gas injection [11−14] and observed that it is an important factor in smelting and material processing.

Ma *et al.* [15] investigated the quantity of slag splashing in a nickel PSC via 1:4 scale cold model experiments. They found that the angle of the tuyere is a significant factor in reducing slag splashing, that is, slag splashing dramatically reduces from 80% to 5% when the tuyere angle varies from −30° to −10°. Rosales *et al.* [16] emphasized that a combined lateral and bottom gas injection method decreases about 50% amplitude of the surface wave in a 1:5 scaled water model of copper PSC. Valencia *et al.* [17] examined the gas−liquid multiphase flow in a Teniente-type copper converter via computational fluid dynamics simulations and cold water experiments. They measured the oscillatory amplitude and frequency of bath movement and obtained a dimensionless equation for the oscillatory frequency. The circulation flow determines the mixing among gas, slag, and matte phases and serves as an important factor of converting efficiency. Zhao *et al.* [18] investigated the circulation flows in PSC under different operating conditions via a numerical simulation approach. They observed that the circular flow is promoted by increasing the gas flow rate and decreasing the nozzle height and diameter. Another significant factor of multiphase stirring and mixing systems is the dead zone. Chibwe *et al.* [19−20] found that the dead zone is close to the sidewall of PSC and associated with poor dissolution rates.

✉ Corresponding author: Hong Yong Sohn E-mail: h.y.sohn@utah.edu

Mixing efficiency is an important indicator in evaluating gas–liquid stirring system. Almaraz *et al.* [21] used a color tracer injected into a PSC cold model and investigated the mixing process in the bath. Wang *et al.* [22] applied particle image velocimetry (PIV) to study the velocity field in a bottom-blown furnace. They then added seeding particles into the bath to evaluate the overall mixing effect. Mixing time is often used to represent the gas–liquid mixing process. Fabritius *et al.* [23] measured the mixing time in a sidewall-blowing converter and observed that the mixing time is shorted by 27% when the blowing practice is changed. Shui *et al.* [24] established a 1:12 scaled-down cold model of a bottom-blown copper smelting furnace. They optimized the operating parameters of the horizontal distance from the blowing lance, detector depth, bath height, and gas flow rate by measuring the mixing times.

In this work, the effects of gas stirring and material mixing in a copper PSC were investigated in a 1:5 scale cold model by applying zone distribution analysis and novel mixing measurement. A dimensionless equation was developed to determine the correlation of the effects of stirring and mixing energy. The optimal conditions of PSC process were obtained by combining the results of zone distribution and mixing time.

2. Experimental

A 1:5 cross-section model with three tuyeres was constructed in accordance with the principles of geometric and dynamic similarities between industrial and experimental PSC [25]. Fig. 1 shows the experimental setup comprising the vessel and tuyeres. All the model dimensions should be scaled down from industrial PSC dimensions at a certain ratio ($\alpha = 0.2$) to satisfy the requirement of geometric similarity. The modified Froude number (Fr') should be the same between the experimental model and the industrial PSC to meet the requirement of fluid dynamic similarity. Fr' is expressed as follows:

$$Fr' = \frac{\rho_g u^2}{\rho_l g H} = \frac{Q^2 \rho_g}{g\rho_l (\pi d^2/4)^2 H} \tag{1}$$

where ρ_g and ρ_l are the gas and liquid densities (kg/m^3), respectively; g is the gravitational acceleration (m/s^2); d is the tuyere diameter (m); H is the liquid height (m); Q is the gas flow rate (m^3/s); and u is the gas injected velocity (m/s) expressed as

$$u = \frac{4Q}{\pi d^2} \tag{2}$$

In this work, the scale factor of 0.2 is expressed as

$$\alpha = \frac{d_M}{d_I} = \frac{H_M}{H_I} \tag{3}$$

where M and I are the experimental model and industrial PSC, respectively.

The modified Froude number Fr'_M and Fr'_I should be equal to ensure the dynamic similarity:

$$Fr'_M = Fr'_I \tag{4}$$

The experimental gas flow rates are calculated as follows:

$$Q_M = \alpha^{2.5} \cdot \left(\frac{\rho_{g,I} \cdot \rho_{l,M}}{\rho_{g,M} \cdot \rho_{l,I}} \right)^{0.5} \cdot Q_I \tag{5}$$

where $\rho_{g,I}$ and $\rho_{l,I}$ are equal to 1.37 kg/m^3 (for 22%–25% oxygen-enriched air at standard temperature and pressure, STP) and 4500 kg/m^3 (for copper), respectively; and $\rho_{g,M}$ and $\rho_{l,M}$ are equal to 1.29 kg/m^3 (for air at STP) and 998 kg/m^3 (for water), respectively. The industrial gas flow rate from 54 tuyeres is 25000–35000 m^3/h (at STP).

The experimental gas flow rate can be calculated in accordance with Eq. (5):

$$Q_M = 0.2^{2.5} \cdot \left(\frac{1.37 \times 998}{1.29 \times 4500} \right)^{0.5} \cdot Q_I = 0.00869 Q_I \tag{6}$$

In this work, a three-tuyere cold model was used, and its thickness, L, was equal to three times the distance of the tuyere spacing (equal to 0.0304 m in the experimental model and 0.152 m in the industrial converter).

In Eq. (6), the calculated Q_M of 54 tuyeres ranges from 217 to 304 m^3/h. Thus, Q_M of the three tuyeres in the cold model is about 12–17 m^3/h. The extended range of Q_M selected in this work is 9–21 m^3/h to optimize the gas flow rate. The dimensions and operating conditions in the experimental apparatus are shown in Fig. 1.

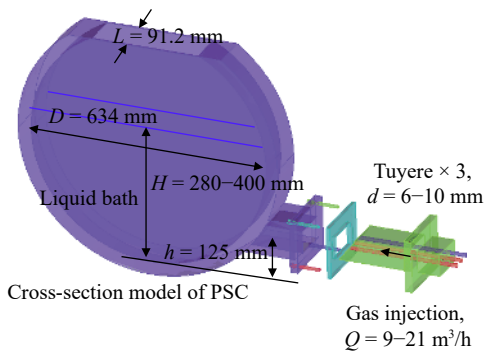

Fig. 1. Experimental model of PSC.

3. Results and discussion

3.1. Relative zone volume distributions

During PSC converting process, the gas injected through the horizontal tuyeres stirs the liquid bath. The flow field distributed in the bath has different characteristics in different regions. In a previous work [25], the liquid bath in PSC is divided into five zones, namely, injection, splashing, strong-loop, weak-loop, and dead zones. Zone distribution largely determines the stirring and mixing effect. In this work, the three key zones, namely, dead, splashing, and strong-loop zones, were quantitatively characterized with an image processing technology. The relative zone volumes were investigated by calculating the area of the approximate alternative geometry (Fig. 2). The zone volumes with errors of <5% were calculated on the basis of the high-definition high-speed pictures. The high-speed pictures were initially sharpened and binarized. Subsequently, the three zones were marked as

rectangles or arcs. The areas of the approximate alternative geometries were used to obtain the areas of the dead zone (S_{dead}), the splashing zone ($S_{splashing}$), and the strong-loop zone ($S_{strong\text{-}loop}$). The area S_i was multiplied by the vessel length (L) to calculate the volumes of the three zones (V_i):

$$V_i = S_i \cdot L \tag{7}$$

where i represents the dead, splashing, and strong-loop zones.

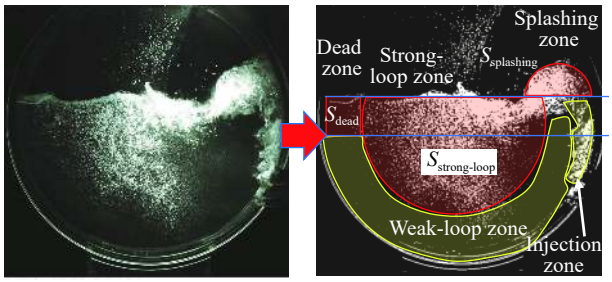

Fig. 2. Schematic of zone volume measurement.

Zone distribution is associated with the energy input of the injected gas flow. In a previous work, the specific mixing power (mixing power per unit mass of liquid, ε_m) in a PSC was composed of the buoyancy specific power (ε_b) and gas kinetic energy (ε_k) expressed as follows [26–27]:

$$\varepsilon_m = \varepsilon_b + \varepsilon_k \tag{8}$$

where ε_b is calculated as

$$\varepsilon_b = \frac{2n_g RT}{W}\ln\left(1+\frac{\rho_l g H_S}{P_a}\right) = \frac{2QP_a}{W}\ln\left(1+\frac{\rho_l g(H-h)}{P_a}\right) \tag{9}$$

where n_g is the number of moles of gas (mol), R is the ideal gas content, T is the gas temperature (K), g is the gravitational acceleration (m/s^2), H_S is the injection submergence (m) that is equal to $H - h$, H is the bath height (m) and h is the tuyere height (m) shown in Fig. 1, W is the bath weight (kg), and P_a is the atmospheric pressure (Pa).

ε_k is determined as follows:

$$\varepsilon_k = \frac{1}{2}\dot{m}_g u^2 = \frac{\rho_g Q^3}{2WnA^2} = \frac{8\rho_g Q^3}{\pi^2 W n d^4} \tag{10}$$

where $\dot{m}_g$ is the mass flow rate of gas (kg/s), u is the gas velocity at the tuyere exit (m/s), n is the number of tuyeres, A is the cross-sectional area (m^2) of the tuyere equal to $\pi d^2/4$.

Fig. 3(a) illustrates the specific mixing power for different tuyeres with different diameters. In Eq. (9), the diameter of the tuyere did not influence ε_b. In Eq. (10), as the diameter of the tuyere increased, the gas kinetic energy and mixing power decreased when other conditions remained unchanged. Fig. 3(b) shows the relative volume distributions which defined as the ratio of volume of dead, splashing and strong-loop zones (V_i) to total volume of the bath (V_{bath}) for different tuyeres with different diameters (d). Their diameter elicited the greatest influence on the strong-loop area, where the gas and liquid reacted the most. The relative volume of the strong-loop zone prepared with 10 mm tuyeres was only half of that with 6 mm tuyeres. Adopting tuyeres with large diameters significantly decreased the strong-loop volume, thereby lowering the converting efficiency. In other words, as d increased, a lower input of the mixing power caused a decrease in the volumes of the splashing and strong-loop zones and an increase in the volume of the dead zone.

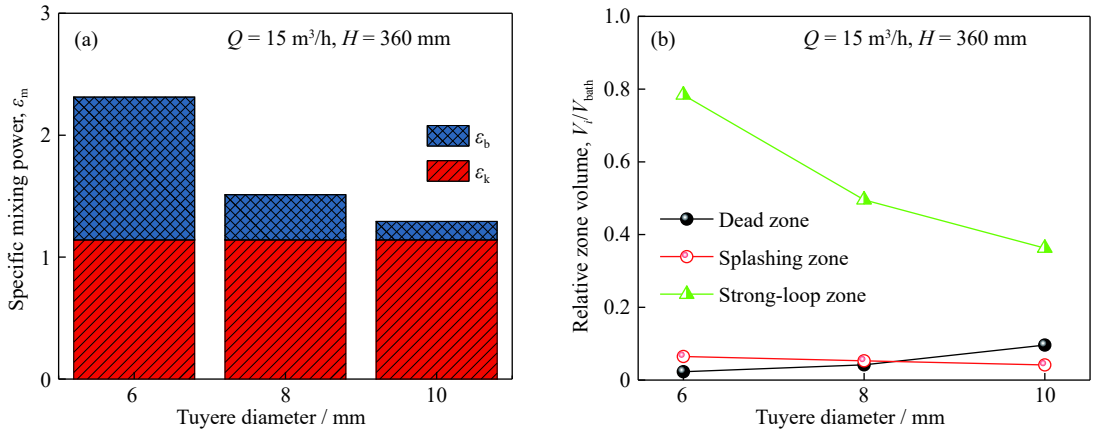

Fig. 3. Specific mixing power (a) and relative zone volumes (b) for different tuyeres with different diameters.

Fig. 4(a) presents the specific mixing power for different liquid heights. As H increased, ε_b decreased, ε_k increased slightly, and ε_m decreased. Fig. 4(b) shows the relative volume distributions of the dead, splashing, and strong-loop zones with different liquid heights (H). In Equation (9), as the liquid height increased, the effective bath weight increased, and the buoyancy specific power (ε_b) decreased. Conversely, as the injection submergence increased, ε_b increased. When H increased from 280 mm to 320 mm, the volume of the strong-loop zone decreased possibly because the increasing buoyancy power could not compensate for the decrease in ε_b caused by the increase in W. When H increased to 360 mm, H_S also increased, and the momentum exchange between the gas and the liquid strengthened. Consequently, the strong-loop area increased. As H further increased, the splashing zone enlarged because of the combination of the gas flow with the long rising path. The large combined bubbles with a rapidly increasing vertical velocity and a decreasing horizontal strength caused ε_b and ε_k to decrease. As W increased and ε_b and ε_k decreased, the volume of the strong-loop zone decreased significantly.

When H was below 360 mm, the volume of the dead zone

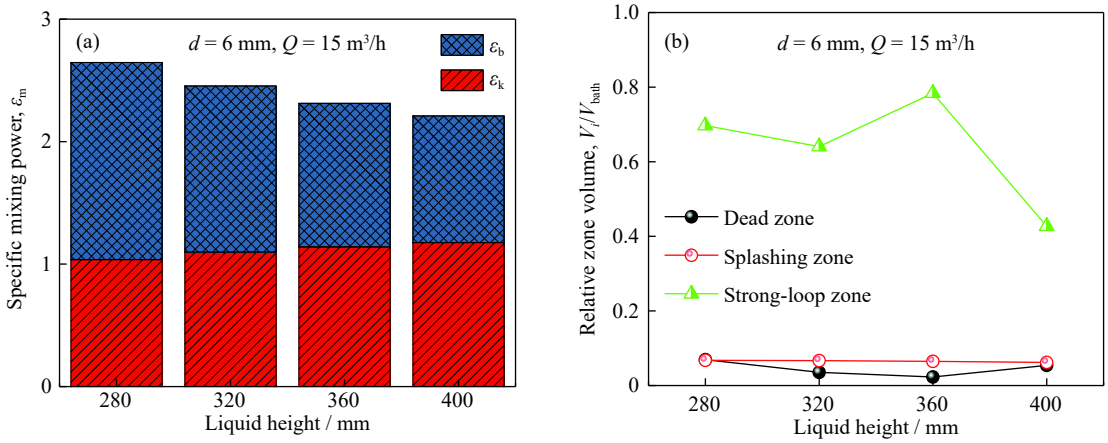

Fig. 4. Specific mixing power (a) and relative zone volumes (b) for different liquid heights.

decreased slightly as H increased. When H increased to 400 mm, the vertical stirring was much larger than the horizontal component, and the development of the strong-loop zone was inhibited. As a result, the volume of the dead zone increased.

Fig. 5(a) shows the specific mixing power for different gas flow rates. As Q increased, ε_b and ε_k increased, thereby rapidly increasing the specific mixing power. Fig. 5(b) illustrates the relative volume distributions of the dead, splashing, and strong-loop zones with different gas flow rates (Q). As Q increased, ε_k increased, as shown in Eq. (10). Consequently, $V_{splashing}$ and $V_{strong\text{-}loop}$ increased, and V_{dead} decreased as shown in Fig. 5(b). However, when Q exceeded 18 m³/h, the bubbles merged into larger ones, and the vertical stirring was strong. Although $V_{splashing}$ did not change remarkably as Q increased, the gas flow decreased in the horizontal direction and increased in the vertical direction. The gas kinetic energy in the splashing zone was not effectively transferred to the strong-loop zone. Thus, $V_{strong\text{-}loop}$ decreased significantly. The weak loop also improved, and the dead zone decreased because of the enhanced stirring and mixing in the bath.

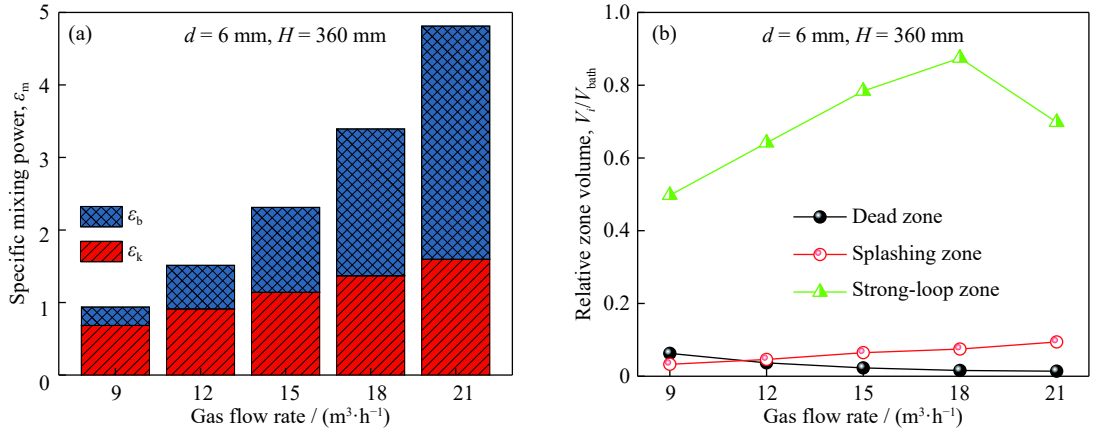

Fig. 5. Specific mixing power (a) and relative zone volumes (b) for different gas flow rates.

3.2. Mixing time

Mixing time is an important and effective factor in evaluating the mixing efficiency. In this study, the mixing time was measured to investigate the stirring and mixing effects related to flow field distribution. A conductive salt solution, such as NaCl solution or KCl solution, is used as a tracer for determining the mixing time in a vessel. However, a liquid tracer cannot represent the properties of solid quartz flux particles. In addition, the densities of common salt particles are 2–5 times that of the liquid in water model experiments. Therefore, special hollow salt microspheres (Tate & Lyle Group, UK), whose density ratio with water was close to that between quartz flux and copper matte, were adopted as the tracer in this study to simulate the movement, melting, and mass transfer processes of the quartz flux particles in the bath [28]. The results revealed that the micron scale of the salt powders had good traceability with the liquid phase.

Mixing time is defined as the time required for achieving a certain degree of homogeneity of an injected tracer in a vessel [29]. It is usually measured with the conductance method. Variations in conductivity are monitored after a tracer is added. The criterion for determining the mixing time in this work was defined as the beginning of the period when the fluctuation in conductivity stabilizes, and its magnitude remains constant for 3–5 min. Fig. 6 presents the diagram of the criterion that produced accurate results even when the amounts of the tracer and the liquid bath vary [30].

In Section 3.1, the distributions of the dead, splashing, and strong-loop zones were essential for the stirring and mixing effects in the bath. Therefore, the tracer was added to these zones and to the injection zone. The dead zone was the slag

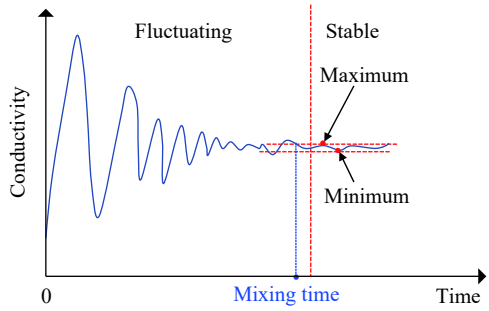

Fig. 6. Measuring criterion of mixing time.

distribution region, and very few chemical reactions occur in this region during the converting process. The bottom measuring point was located in the weak loop region, where chemical reactions and mass transport were slow, and the mixing time at this point was more representative than that at other points. Thus, one position on the vessel bottom was selected as the measuring point (Fig. 7). Then, 10 g of the solid tracer was added from the tracer injection point for each test, and conductivity was determined at the measuring point for 5 min. Each test was repeated five times, and the average mixing time was calculated.

Fig. 8 shows the mixing time with different diameters of tuyeres. As d increased, the specific mixing power decreased from the value in Fig. 3(a) because of the decrease in the kinetic energy of the injected gas. Therefore, the mixing degrees in the bath decreased, causing the mixing time to increase at all four positions. With a large diameter (d = 8 and 10 mm),

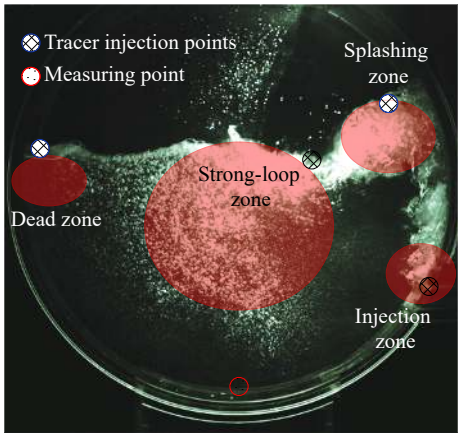

Fig. 7. Tracer injection and measuring positions.

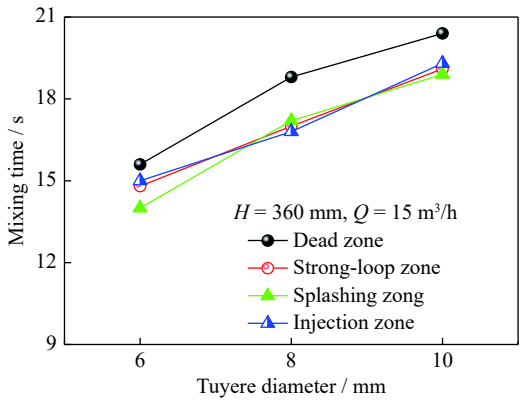

Fig. 8. Mixing time for different diameters of tuyeres.

the buoyancy specific power was the main driving force, so the mixing time changed slightly as tracers were added at the injection, splashing, and strong-loop zones. As d decreased to 6 mm, the injected gas kinetic energy increased and caused a decrease in mixing time with tracer addition at the injection zone. The mixing time in the dead zone was the longest because of the weaker fluid flow than in the three other zones.

Fig. 9 shows the mixing time with different liquid heights. At a low H of 280 mm, the mixing time in the dead zone was larger than that in the other zones because of the large volume of the dead zone. As H increased, the mixing times in all cases decreased although the amount of liquid increased. In Fig. 4(a), an increase in H caused a decrease in the specific mixing power. At a low H of 280 mm, the energy utilization efficiency was low because of the short interaction time between the gas and the liquid although the largest values of the specific mixing power and relative volume of the strong-loop zone were obtained. Therefore, the mixing time was large. When H increased to 320–400 mm, the specific mixing power and relative volume of the strong-loop zone decreased slightly, but the energy utilization efficiency increased. Consequently, the mixing time shortened. Therefore, increasing H in a certain region did not reduce the stirring and mixing effects that benefited from an increase in the energy utilization of the injected gas. As H further increased to 400 mm, the mixing time in the four regions behaved differently because of the energy attenuation with a long-term momentum exchange between the gas and the liquid during the gas-blowing process. The gas injected through the tuyere elevated and escaped from the bath surface, thereby generating a splashing wave, which flowed back to the bath and generated the strong-loop. With energy attenuation, the strong-loop zone decreased, and the dead zone increased greatly. As a result, the mixing time was extended when the tracer was added to dead zone. With an increase in H, the inputted energy attenuated successively and reduced the mixing in the injection, splashing, strong-loop, and dead zones.

Fig. 10 illustrates the mixing time with different gas flow rates. At a low gas flow rate of 9 m^3/h, the mixing time decreased successively in the injected, splashing, strong-loop, and dead zones. As Q increased to 12 m^3/h, the specific mixing power increased, and the differences in the mixing time in the splashing, strong-loop, and dead zones were reduced.

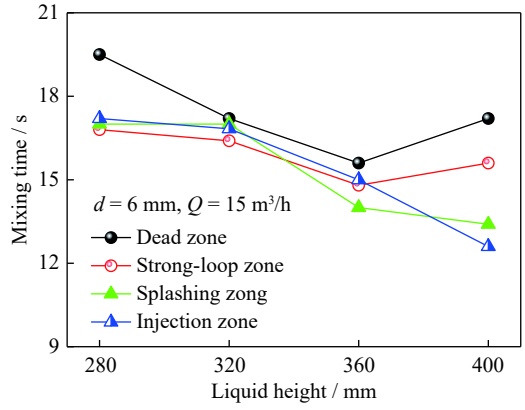

Fig. 9. Mixing time for different liquid heights.

Conversely, the mixing time increased when the tracer added at the injection zone because of the movement of tracer particles with a large ring bubble. When Q increased to 12–15 m^3/h, effective stirring and mixing were still not achieved in the bath although the specific mixing power increased. Furthermore, splashing strengthened, and the number of large bubbles increased. Consequently, the mixing time was prolonged. The best mixing effect was obtained when Q increased to 18 m^3/h. As Q (21 m^3/h) further increased, the mixing times in the splashing and strong-loop zones (at the backflow point of the splashing wave) were extended significantly. This observation might be attributed to the movement of the tracer out of the bath with the splash, its adherence to the side wall of the vessel, and its gradual return to the bath. The shortest mixing time was found in the injection zone.

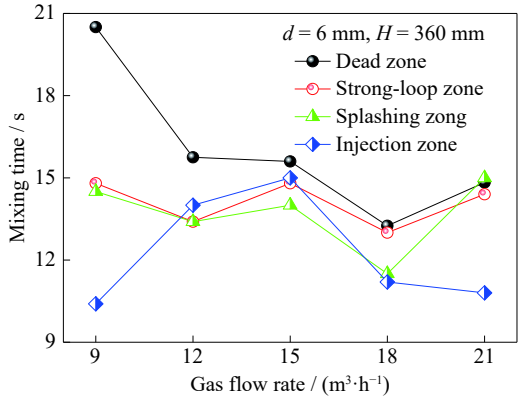

Fig. 10. Mixing time for different gas flow rates.

During the converting process, quartz flux becomes fed into the molten bath and reacts with FeO and Fe_3O_4 to form the slag phase [31]. The quartz flux participates in the reaction only with the liquid slag phase and does not directly react with the gas phase. As such, its addition position and distribution in the molten bath are essential for slag making. In traditional slag making, quartz flux is added directly from the mouth of the top furnace by using a crane hopper, which causes a long smelting time and difficulty in controlling because of magnetite formation. Magnetite increases slag viscosity and causes difficulty in separating slag and copper [32]. The mixing results indicated that the best way to obtain the shortest mixing time was injecting the quartz flux through the tuyeres. This process would provide excellent mixing effects, improve the slag-making reaction rate, and inhibit magnetite formation. This flux injection technique has been tested on a nickel PSC in Kalgoorlie Nickel Smelter, and a good slag-making effect has been obtained [33]. However, the technique should still be further developed to an engineered system. In particular, refractory bricks surrounding a flux injection tuyere fail quickly, so refractory materials and injection should be improved.

3.3. Dimensionless correlation

The relative strength of the stirring and mixing energy can be expressed as $\gamma = V_{splashing}/(V_{bath} - V_{dead})$, where $V_{splashing}$ is approximately the input stirring kinetic energy, and ($V_{bath} - V_{dead}$) is the stirring and mixing energy in the bath. In this section, the dimensionless equation of γ as a function of operating parameters in terms of the Froude number (Fr), H/D, and d/D was established:

$$\gamma = \frac{V_{splashing}}{V_{bath} - V_{dead}} = f(Fr, H/D, d/D) \tag{11}$$

where D is the diameter of the Peirce–Smith converter. γ under different operating conditions was calculated on the basis of the experimental data on zone volumes shown in Section 3.1 (Table 1).

Table 1. Dimensionless parameters in the bath

Q / ($m^3 \cdot h^{-1}$)	Fr	γ	H / m	H/D	γ	d / m	d/D	γ
9	14773	0.035	0.28	0.442	0.073	0.006	0.0095	0.066
12	26263	0.048	0.32	0.505	0.069	0.008	0.0126	0.055
15	41037	0.066	0.36	0.568	0.066	0.010	0.0158	0.046
18	59093	0.076	0.40	0.631	0.115			
21	80432	0.083						

The allometric power functions in the following correlation equation were selected to fit the dimensionless data:

$$\gamma = \frac{V_{splashing}}{V_{bath} - V_{dead}} = K \times Fr^a \times \left(\frac{H}{D}\right)^b \times \left(\frac{d}{D}\right)^c \tag{12}$$

The calculated best-fit values of a, b, and c were 0.57, −038, and −0.70, respectively. The constant K was equal to 4.7×10^{-6}. Thus, the dimensionless equation of γ is given by

$$\gamma = \frac{V_{splashing}}{V_{bath} - V_{dead}} = 4.7\times10^{-6} \times Fr^{0.57} \times \left(\frac{H}{D}\right)^{-0.38} \times \left(\frac{d}{D}\right)^{-0.70} \tag{13}$$

Fig. 11 shows the verification between the correlation and experimental data. This result revealed a good agreement with errors of <5% and indicated that the dimensionless equation of γ could represent the degree of the stirring performance of the PSC.

4. Conclusions

(1) The equation of the specific mixing power could represent the mixing effect and flow field distribution, including dead, splashing, and strong-loop zones. However, at a high liquid height (400 mm) and a high gas flow rate (21 m^3/h), the energy dissipated largely because of the strong surface splashing. The specific mixing power, including buoyancy

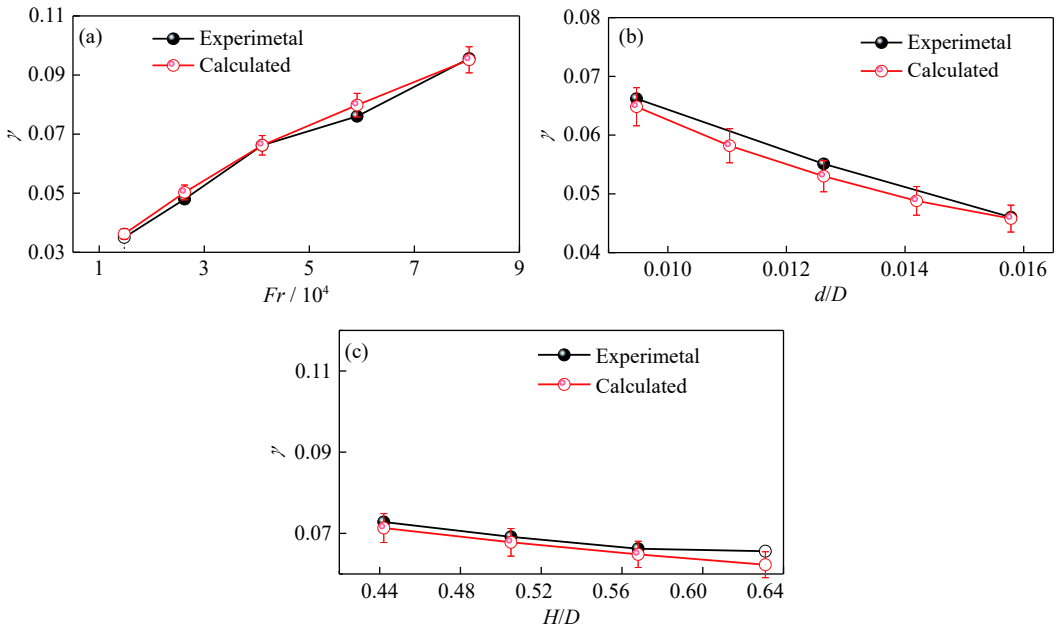

Fig. 11. Verification between the correlated and experimental values of γ.

specific power and gas kinetic energy, should be considered in evaluating the specific mixing power in the bath. A dimensionless equation expressed as $\gamma = 4.7 \times 10^{-6} \times Fr^{0.57} \times (H/D)^{-0.38} \times (d/D)^{-0.70}$ represented the mixing effect with an error of <5%.

(2) The mixing time in the injection, splashing, strong-loop, and dead zones showed a successively decreasing trend, especially under the following conditions: large H of 400 mm and low Q of 9 m^3/h. At a high Q of 21 m^3/h, the mixing time was prolonged because of the strong surface splashing in the splashing and strong-loop zones.

(3) The slag made by adding quartz flux to the backflow point of the splashing wave through a chute without rotating the converter was better than that traditionally prepared by adding the flux through the top opening by using a crane hopper. The best way was injecting the flux through tuyeres if the erosion of a tuyere firebrick could be resolved.

Acknowledgements

This work was financially supported by the National Natural Science Foundation of China (No. 51974018), the Guangxi Innovation-Driven Development Project (No. AA18242042-1), and the Fundamental Research Funds for the Central Universities (No. FRF-TP-19-016A3). Hongliang Zhao was also grateful to the China Scholarship Council for the Chinese Government Scholarship granted to Hongliang Zhao for studying as a visiting scholar at Professor Hong Yong Sohn's laboratory at the University of Utah in USA.

Conflict of Interest

The authors declare that they have no known competing financial interests or personal relationships that could have appeared to influence the work reported in this paper.

References

[1] Z.H. Liu and L.G. Xia, The practice of copper matte converting in China, *Miner. Process. Extr. Metall.*, 128(2018), No. 1-2, p. 117.

[2] P. Taskinen, G. Akdogan, I. Kojo, M. Lahtinen, and A. Jokilaakso, Matte converting in copper smelting, *Miner. Process. Extr. Metall.*, 128(2018), No. 1-2, p. 58.

[3] Y.A. Korol and S.S. Naboychenko, The tuyere in a protective shell to convert the nickel and copper mattes, *Non-ferrous Met.*, 2018, No. 2, p. 3.

[4] J.J. Wang, L.F. Zhang, G. Cheng, Q. Ren, and Y. Ren, Dynamic mass variation and multiphase interaction among steel, slag, lining refractory and nonmetallic inclusions: Laboratory experiments and mathematical prediction, *Int. J. Miner. Metall. Mater.*, 28(2021), No. 8, p. 1298.

[5] J. Ma, Y.P. Song, P. Zhou, W. Cheng, and S.G. Chu, A mathematical approach to submerged horizontal buoyant jet trajectory and a criterion for jet flow patterns, *Exp. Therm. Fluid Sci.*, 92(2018), p. 409.

[6] J. Vaarno, J. Pitkälä, T. Ahokainen, and A. Jokilaakso, Modelling gas injection of a Peirce–Smith-converter, *Appl. Math. Modell.*, 22(1998), No. 11, p. 907.

[7] Q.F. Hou, D.Y. E, and A.B. Yu, Discrete particle modeling of lateral jets into a packed bed and micromechanical analysis of the stability of raceways, *AIChE J.*, 62(2016), No. 12, p. 4240.

[8] D.Y. E, Validation of CFD–DEM model for iron ore reduction at particle level and parametric study, *Particuology*, 51(2020), p. 163.

[9] D.Y., E, Numerical investigation of mixed layer effect on permeability in a dynamic blast furnace, *Eng. Rep.*, 2(2020), No. 5, art. No. e12166.

[10] L.M. Wang, S.H. Yin, and A.X. Wu, Visualization of flow behavior in ore-segregated packed beds with fine interlayers, *Int. J. Miner. Metall. Mater.*, 27(2020), No. 7, p. 900.

[11] G.W. Tang, A.K. Silaen, H.J. Yan, Z.X. Cui, Z. Wang, H.B. Wang, K.L. Tang, P. Zhou, and C.Q. Zhou, CFD study of gas-liquid phase interaction inside a submerged lance smelting furnace for copper smelting, [in] *Proceedings of 8th International Symposium on High-Temperature Metallurgical Processing*, San Diego, 2017, p. 101.

[12] H. Chen, J. Ma, and H.T. Liu, Least square spectral collocation method for nonlinear heat transfer in moving porous plate with convective and radiative boundary conditions, *Int. J. Therm. Sci.*, 132(2018), p. 335.
[13] Y. Xue, F.N. Dang, Z.Z. Cao, F. Du, F. Liu, J. Ren, and F. Gao, Numerical analysis of heat and gas transfer characteristics during heat injection processes based on a thermo-hydro-mechanical model, *Energies*, 11(2018), No. 7, art. No. 1722.
[14] Z. Chen and H.F. Shen, Simulation of macrosegregation in a 36-t steel ingot using a multiphase model, *Int. J. Miner. Metall. Mater.*, 27(2020), No. 2, p. 200.
[15] D.G. Ma, W.Q. Chen, and X.M. Che, Physical modelling of slag splashing in nickel converter, *Can. Metall. Q.*, 51(2012), No. 1, p. 31.
[16] M. Rosales, A. Valencia, and R. Fuentes, A methodology for controlling slopping in copper converters by using lateral and bottom gas injection, *Int. J. Chem. React. Eng.*, 7(2009), No. 1, p. 1.
[17] A. Valencia, M. Rosales, R. Paredes, C. Leon, and A. Moyano, Numerical and experimental investigation of the fluid dynamics in a Teniente type copper converter, *Int. Commun. Heat Mass Transf.*, 33(2006), No. 3, p. 302.
[18] H.L. Zhao, X. Zhao, L.Z. Mu, L.F. Zhang, and L.Q. Yang, Gas−liquid mass transfer and flow phenomena in a Peirce-Smith converter: A numerical model study, *Int. J. Miner. Metall. Mater.*, 26(2019), No. 9, p. 1092.
[19] D.K. Chibwe, G. Akdogan, and J. Eksteen, Solid−liquid mass transfer in a Peirce−Smith converter: A physical modelling study, *Metall. Min. Ind.*, 3(2011), No. 5, p. 202.
[20] D.K. Chibwe, G. Akdogan, P. Taskinen, and J.J. Eksteen, Modelling of fluid flow phenomena in Peirce−Smith copper converters and analysis of combined blowing concept, *J. S. Afr. I. Min. Metall.*, 115(2015), No. 5, p. 363.
[21] A. Almaraz, C. López, M.A. Barrón, and G. Plascencia, Numerical and physical modeling of turbulence in a Peirce−Smith copper converter, *J. Mater. Sci. Eng.*, 3(2013), No. 7, p. 510.
[22] D.X. Wang, Y. Liu, Z.M. Zhang, T.A. Zhang, and X.L. Li, PIV measurements on physical models of bottom blown oxygen copper smelting furnace, *Can. Metall. Q.*, 56(2017), No. 2, p. 221.
[23] T. Fabritius, P. Kupari, and J. Harkki, Physical modelling of a sidewall-blowing converter, *Scand. J. Metall.*, 30(2001), No. 2, p. 57.
[24] L. Shui, Z.X. Cui, X.D. Ma, M. Akbar Rhamdhani, A. Nguyen, and B.J. Zhao, Mixing phenomena in a bottom blown copper smelter: A water model study, *Metall. Mate. Trans. B*, 46(2015), No. 3, p. 1218.
[25] X. Zhao, H.L. Zhao, L.F. Zhang, and L.Q. Yang, Gas−liquid mass transfer and flow phenomena in the Peirce–Smith converter: A water model study, *Int. J. Miner. Metall. Mater.*, 25(2018), No. 1, p. 37.
[26] D.K. Chibwe, G. Akdogan, C. Aldrich, and R.H. Eric, CFD modelling of global mixing parameters in a Peirce–Smith converter with comparison to physical modelling, *Chem. Prod. Process Model.*, 6(2011), No. 1, p. 22.
[27] H. Turkoglu and B. Farouk, Mixing time and liquid circulation rate in steelmaking ladles with vertical gas injection, *ISIJ Int.*, 31(1991), No. 12, p. 1371.
[28] H.L. Zhao, P. Yin, L.F. Zhang, and S. Wang, Water model experiments of multiphase mixing in the top-blown smelting process of copper concentrate, *Int. J. Miner. Metall. Mater.*, 23(2016), No. 12, p. 1369.
[29] G. Ascanio, Mixing time in stirred vessels: A review of experimental techniques, *Chinese J. Chem. Eng.*, 23(2015), No. 7, p. 1065.
[30] H.L. Zhao, L.F. Zhang, P. Yin, and S. Wang, Bubble motion and gas-liquid mixing in metallurgical reactor with a top submerged lance, *Int. J. Chem. React. Eng.*, 15(2017), No. 3, p. 1.
[31] M. Shamsuddin and H. Y. Sohn, Constitutive topics in physical chemistry of high-temperature nonferrous metallurgy - A review: Part 1. Sulfide roasting and smelting, *JOM*, 71(2019), No. 9, p. 3253.
[32] I. Bellemans, E. De Wilde, N. Moelans, and K. Verbeken, Metal losses in pyrometallurgical operations - A review, *Adv. Colloid. Interface Sci.*, 255(2018), p. 47.
[33] C.P. Culshaw, A.G. Hunt, and M. Nilmani, Injection of silica flux to a nickel converter through a submerged tuyere, [in] *Converting, Fire Refining and Casting: Proceedings of a Symposium Sponsored by the Extraction and Processing Division, Prometallurgical Committee*, Francisco, 1993, 79.